Basic circuit element for the implementation of base-3 and base-4 algorithms realized by an asymmetric MgO-based double-barrier magnetic tunnel junction

Xing-tao Jia,[1] Ping-Ping Wu,[1] Li-Wei Zhang,[1] and Hui-Min Tang[2]
[1] *School of Physics and Electronic Information Engineering, Henan Polytechnic University, Jiaozuo 454000, China*
[2] *School of Physical Science and Technology, Guangxi Normal University, Guangxi 541001, China*

(Received 14 January 2019; revised manuscript received 5 May 2019; published 15 May 2019)

We study the resistance states and spin dynamics in a Ag/Fe(8)/MgO(3)/Fe(8)/MgO(5)/Fe/Ag junction based on a first-principles scattering theory. Spin dynamics simulations show that up to four resistance states with noticeable difference can be achieved via manipulating the voltage bias scheme and the position of the reference magnetization. The study indicates possible multiple-valued logic applications in an asymmetric MgO-based double-barrier magnetic tunnel junction.

DOI: 10.1103/PhysRevB.99.174413

I. INTRODUCTION

Multiple-valued logic (MVL) applications such as multi-bit storage [1–11] and neuromorphic computing [4,7,12–16] have achieved much attention recently. Traditional computer systems use binary logic for their operations for the simplicity and stability. The use of the MVL not only helps to improve the efficiency of the arithmetic operations [17,18] but also reduces the complexity of the computing architecture [19]. The intermediate states can be regarded as uncertainty states. For example, a ternary number (base-3) can be represented by $\{-1, 0, 1\}$, where 0 can stand for an uncertainty state. The introduction of the uncertainty state [20] makes the MVL algorithm more natural to simulate brain intelligence. The MVL applications can be realized by using magnetic tunnel junctions (MTJs) with ferroelectric barriers [2,3], memristive effect of the tunnel junction [1,4,5,7], multilevel cell spin transfer torque random access memory (STT-RAM) [8,9], a moving domain wall in the tunnel junction [10], planar Hall resistance [11], and the negative differential resistance (NDR) effect in two-dimensional (2D) materials based heterostructure [19,21].

Magnetic tunnel junction is a good candidate for MVL applications [1,4,6,7,10,14,16] for large tunnel magnetoresistance ratios (TMRs). Single-barrier MTJ (SMTJ) possesses two stable resistance states, which can be represented as "on" and "off" binary logic. Memristive effect enables more resistance states in the SMTJ than present MVL applications [1,4,6,10]. The oscillation states of the SMTJ can be used to mimic volatile synapses [14] and large-scale neural networks [16]. The good compatibility to the state-of-art semiconductor technique, high endurance, low energy consumption, and good scalability make MgO-based SMTJ a good candidate as the basis circuit element for the implementation of neuromorphic computing [15]. Compared with the SMTJ, the double-barrier MTJ (DMTJ) can possess more resistance states, which can be found in MVL applications naturally. More parameter space, such as the thickness of barrier and sandwiched ferromagnet, position of the reference magnetization, voltage bias scheme, and so on, enable rich spin dynamics behaviors in the DMTJ.

A perpendicular magnetized (PM) structure is favorable for the memory applications; it shows merits of lower switching current density compared with magnetic structure with in-plane anisotropy. Spin torque effects including STT effect [22,23] and spin-orbit torque (SOT) effect [24–36], are favorable to manipulate the magnetic structure electrically [37]. With the aid of an effective field created by the contacted materials [30–33,36], SOT effect can switch the PM structure deterministically. The interplay of STT and SOT can considerably reduce the switching current to an order of 10^6 A cm^{-2} in a MgO-based junction with PM structure [35].

In this paper, we report on theoretical studies on the spin transport and spin dynamics in an asymmetric Ag/Fe/MgO(3)/Fe/MgO(5)/Fe/Ag junction with PM structure. The results show that up to four resistance states in the asymmetric DMTJ with noticeable difference can be manipulated by the voltage bias scheme and the position of the reference magnetization.

II. CALCULATIONS DETAILS

Considering a magnetic multilayer as shown in Fig. 1, the ith magnetization is dynamically coupled with the adjacent magnetizations with a coupled Landau-Lifshitz-Gilbert equation:

$$\dot{\boldsymbol{m}}_i + \hat{\alpha}_i \boldsymbol{m}_i \times \dot{\boldsymbol{m}}_i = \boldsymbol{\Gamma}_i^a - \sum_{j \neq i} \boldsymbol{\Gamma}_j^E + \boldsymbol{\Gamma}_i^T, \quad (1)$$

where $\boldsymbol{m}$ is the unit vector of the magnetization, Γ^a, $\boldsymbol{\Gamma}_i^T$, and Γ^T on the right-hand side are torques exerted on magnetizations, and tensor $\hat{\alpha}$ is the magnetic damping constant including part from the spin-orbit coupling (SOC) effect α_0 and part from interfacial enhancement $\hat{\alpha}'$. $\Gamma^a = \gamma \boldsymbol{m} \times \mathbf{H}$ originates from the magnetocrystalline anisotropy including the uniaxial anisotropy and planar anisotropy. The spin dynamics of the magnetic layers would pump spin current. When the ith magnetization absorbs the spin current, a torque exerted on the ith magnetization is $\boldsymbol{\Gamma}_i^E = \Gamma_{i-1}^E + \Gamma_{i+1}^E$ with $\Gamma_{i-1}^E = \hat{\alpha}'_{F_{i-1}/N_i} \boldsymbol{m}_{i-1} \times \dot{\boldsymbol{m}}_{i-1}$ and $\Gamma_{i+1}^E = \hat{\alpha}'_{F_{i+1}/N_{i+1}} \boldsymbol{m}_{i+1} \times \dot{\boldsymbol{m}}_{i+1}$. $\boldsymbol{\Gamma}^T$ is spin transfer torque, which can be composed

 ©2019 American Physical Society

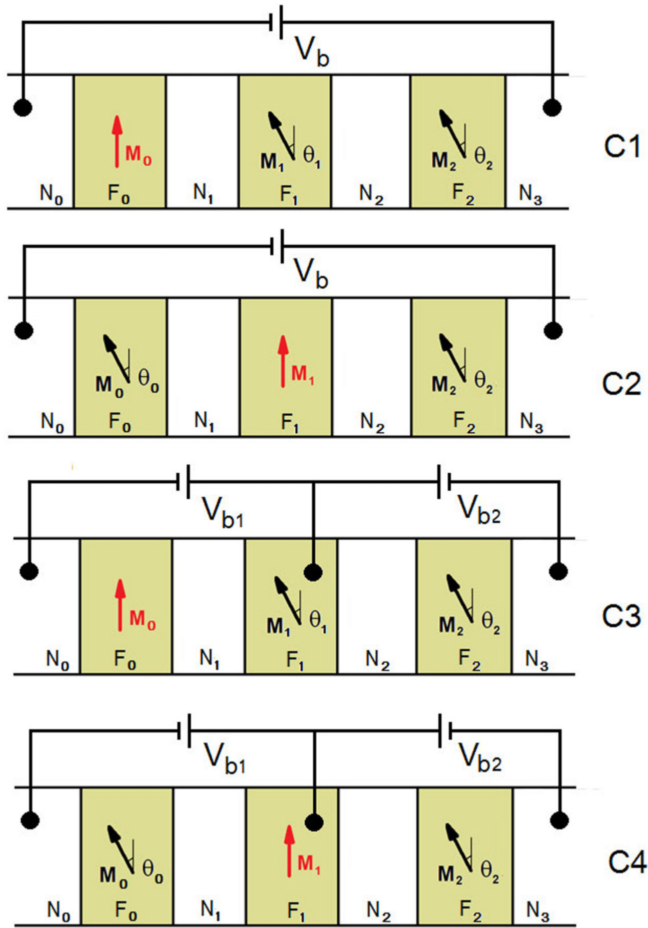

FIG. 1. Schematic N/F/N/F/N/F/N multilayers used in the study, where F and N stand for ferromagnet and nonmagnet, respectively. Four cases, labeled as C1, C2, C3, and C4, respectively, are studied according to the voltage bias scheme and the position of the reference magnetization. Therein, the red (black) arrows stand for fixed (free) magnetizations. The fixed magnetizations are set along the quantum axis. The left-side (L), middle-side (M), and right-side (R) magnetizations show relative angles of θ_0, θ_1, and θ_2 with respect to the quantum axis.

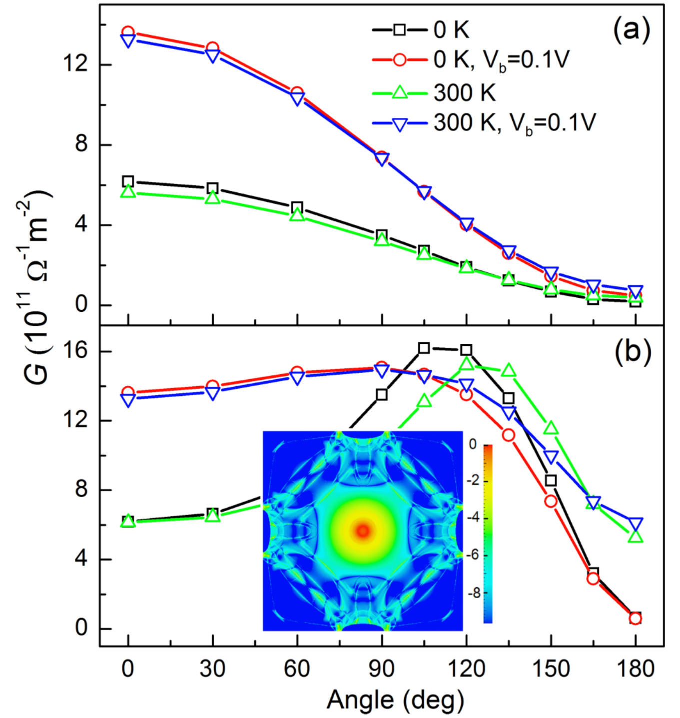

FIG. 2. Angular dependency of the tunneling conductance in the clean Ag/Fe(8)/MgO(3)/Fe(8)/MgO(5)/Fe(8)/Ag DMTJ with (a) fixed $\theta_0 = \theta_1 = 0$ and free θ_2 and (b) fixed $\theta_0 = 0$ and free $\theta_1 = \theta_2$. Inset of (b): $k_\parallel$-dependent conductance in the DMTJ with $T = 0$ K and $V_b = 0$ V at a relative angle of 105°.

of an in-plane and out-of-plane contribution $\mathbf{\Gamma}_i^T = \tau_i^\parallel + \tau_i^\perp$ with $\tau_i^\parallel = \tau_{i,i-1}^\parallel(\boldsymbol{m}_{i-1} \times \boldsymbol{m}_i) + \tau_{i,i+1}^\parallel(\boldsymbol{m}_{i+1} \times \boldsymbol{m}_i)$ and $\tau_i^\perp = \tau_{i,i-1}^\perp \boldsymbol{m}_i \times (\boldsymbol{m}_{i-1} \times \boldsymbol{m}_i) + \tau_{i,i+1}^\perp \boldsymbol{m}_{i+1} \times (\boldsymbol{m}_{i+1} \times \boldsymbol{m}_i)$. For the ith magnetization, both the right-side and the left-side interfaces contribute to the enhanced magnetic damping $\hat{\alpha}'_i = \hat{\alpha}'_{F_i/N_i} + \hat{\alpha}'_{F_i/N_{i+1}}$ with $\hat{\alpha}'_{F_i/N_i} = \frac{\gamma\hbar\hat{g}_{F_i/N_i}\hat{g}_{F_{i-1}/N_{i-1}}}{4\pi M_s V_{F_i}(\hat{g}_{F_i/N_i}+\hat{g}_{F_{i-1}/N_{i-1}})}$ and $\hat{\alpha}'_{F_i/N_{i+1}} = \frac{\gamma\hbar\hat{g}_{F_i/N_i}\hat{g}_{F_{i+1}/N_{i+1}}}{4\pi M_s V_{F_i}(\hat{g}_{F_i/N_i}+\hat{g}_{F_{i+1}/N_{i+1}})}$, where $\hat{g}$ is the effective mixing conductance [38] at the F/N interfaces, M_s is the saturation magnetization, and V_F is the volume of the magnetic layers. The enhanced magnetic damping $\hat{\alpha}'$ can be calculated from first principles [39–42]:

$$\alpha'_{ij} = \frac{\gamma\hbar}{4\pi M_s V_F} \int dk\, \mathbf{Re}\{\mathrm{Tr}[\partial_{m_i} S^\dagger(k) \partial_{m_j} S(k)]\}, \quad (2)$$

where S is the scattering matrix with $i(j) = x, y, z$ for the Cartesian coordinate system and $i(j) = \theta, \phi, r$ for the spherical coordinates system. At finite temperature, the thermal Gilbert damping α^T should count the effect of thermal lattice disorder [43,44]. The calculation details can be found elsewhere [45].

Here, we consider an asymmetric MgO-based DMTJ composed of three Fe layers separated by two MgO barriers. According to the voltage bias scheme and the position of the fixed magnetization, there are four cases labeled as C1, C2, C3, and C4, respectively, as shown in Fig. 1. C1 and C2 are two-terminal (2T) structures, and one voltage bias is exerted on two MgO barriers. C3 and C4 are three-terminal (3T) structures, and voltage biases are exerted on the MgO barriers independently. The self-consistent calculations are performed with the tight-binding linear muffin-tin orbital surface Green's function method with coherent potential approximation to deal with the interfacial disorder [46]. During the electronic structure and transport calculations, we neglect the minor lattice mismatch at the Fe/MgO interface and fix the interfacial atoms at their bulk positions. For the disordered interface, we assume oxygen vacancies (OVs) existed only at the first MgO layer attached to Fe. In the transport calculations, a 1600×1600 k mesh is used to sample the two-dimensional Brillouin zone (2D BZ) for the clean structures to ensure good numerical convergence. Resonant hot spots from the quantum well states and interfacial states in the majority spin channel dominate the conductance, as shown in the inset of Fig. 2, which is easy to converge. The hot spots from the interfacial resonant states in the minority spin channel dominate the enhanced magnetic damping; a much denser k mesh should be used to get convergence. For the imperfect structures,

TABLE I. Tunneling conductance G in units of $10^{11}\ \Omega^{-1}\,\mathrm{m}^{-2}$ and relative magnetoresistance ratio MR in the Ag/Fe(8)/MgO(3)/Fe(8)/MgO(5)/Fe(8)/Ag junction in the absence (presence) of 5% OV at Fe/MgO interfaces. For comparison, the Ag/Fe(8)/MgO/Fe(8)/Ag junction with 3L and 5L MgO barriers are given also.

Structures	0 K		RT	
	G	MR (%)	G	MR (%)
$uuu\,(ddd)$	6.2(6.9)	3150(115)	5.6	1070
$uud\,(ddu)$	0.19(3.2)		0.48	
$udu\,(dud)$	0.35(3.6)	86(13)	0.84	75
$udd\,(duu)$	0.64(7.2)	240(125)	4.4	820
Fe/MgO(3)/Fe	98(210)	930(71)	17	810
Fe/MgO(5)/Fe	6.7(11)	2900(25)	0.45	980

we use a 7×7 supercell and 40×40 k mesh, and over 20 configurations are averaged. More numerical details of the electronic structure and transport calculations can be found elsewhere [47,48].

III. RESULTS AND DISCUSSION

The spin transport in the MTJ decreases exponentially as the barrier thickness increases. To manipulate the magnetic structure electronically, the barrier thickness should not be too thick. There are presented four stable resistance states in the DMTJ, which can be labeled as $uuu\,(ddd)$, $uud\,(ddu)$, $udu\,(dud)$, and $udd\,(duu)$, respectively. Here, the left/middle/right symbol represents the magnetization orientation of the left/middle/right-side magnetic layer, which is parallel (u) or antiparallelg (d) to the spin-quantum axis. For symmetric DMTJ, the $uud\,(ddu)$ and $udu\,(dud)$ states are degenerate, and presents three resistance states only. For asymmetric DMTJ, four resistance states would be presented. Here, we focus on the asymmetric DMTJ with an ultrathin barrier.

A. Resistance states

The quantum well (QW) states in the DMTJ would enhance the conductance noticeably, which is sensitive to the thickness of sandwiched metal [49–52]. For the asymmetric Ag/Fe(8)/MgO(3)/Fe/MgO(5)/Fe(8)/Ag junction, where the numbers in parentheses indicate the thickness in atomic layers (L), the largest conductance of $2.2 \times 10^{12}\ \Omega^{-1}\,\mathrm{m}^{-2}$ is found in a junction with 4 L sandwiched Fe, which decreases to $6.2(2) \times 10^{11}\ \Omega^{-1}\,\mathrm{m}^{-2}$ in a junction with 8(12) L sandwiched Fe. Here, we focus on the junction with moderate 8 L Fe (1.2 nm), which is believed to be perpendicular magnetized [53,54].

Table I shows the resistance states in the asymmetric Ag/Fe(8)/MgO(3)/Fe(8)/MgO(5)/Fe(8)/Ag junction, wherein the relative magnetoresistance ratio is defined as $\mathrm{MR} = [G - \min(G)]/\min(G)$ with the conductance $G = (e^2/h)\mathrm{Tr}(tt^\dagger)$, and t is the transmission part of the scattering matrix. Among the four resistance states, the $uud\,(ddu)$ state shows the largest resistance, which is chosen as the reference state. At zero temperature, the clean junction shows relative MRs ranging from 86% to 3150% with noticeable difference. The interfacial disorders would noticeably enhance the diffusive scattering and deteriorate the specular scattering [47,55], leading to enhancement of the conductance of the antiparallelling states. For the dirty junction with 5% OV at all Fe/MgO interfaces, detailed studies show that the diffusive scattering should amount to around 96% and 99.9% of the total transmission of the uuu and uud structures, respectively. As a result, the relative MRs of the dirty junction are almost one order smaller compared with the clean junctions, and are far less distinguishable. The results are well consistent with our previous study [55]. So, to achieve distinguishable MRs in the DMTJ, the junction should be as clean as possible.

Thermal lattice disorder can enhance the diffusive scattering and deteriorate the specular scattering also, leading to a noticeable change in the relative MRs. Comparing the conductance of the uuu state at room temperature (RT) with that at zero temperature (0 K), we can estimate that the deterioration of the specular scattering would exceed the enhancement of diffusive scattering. We observe that the largest relative MRs at room temperature are about one-third of that at zero temperature. The calculations are well consistent with the experimental studies [56]. Different from junctions with thicker barriers, the ultrathin SMTJ with 3L MgO is not so sensitive to the thermal disorder; this indicates that the thermal lattice disorder of the barriers shows a larger effect than that of the metal layers.

Figure 2 gives the angular dependency of conductance of the clean Ag/Fe(8)/MgO(3)/Fe(8)/MgO(5)/Fe(8)/Ag junction. Two cases are calculated here: one case sets the left magnetization fixed while the middle and right magnetizations are free; another case sets the left and middle magnetizations fixed while the right magnetization is free. The conductance in the first case can be fitted by the $\cos^2(\theta/2)$ function, while large deviations from the theoretical relation are found in the conductance of the second case. The formation of the new resonant states around the center of the 2D BZ, as shown in the inset of Fig. 2, as the relative angle changes should be responsible for the strange angular dependency of the conductance. Thermal lattice disorder at room temperature reduces the conductance at smaller relative angles but enhances the conductance at larger relative angles for both cases, which shows a larger effect in the latter case than in the former case, for both voltage bias $V_b = 0$ and $V_b = 0.1$ V. Considering the relation of the in-plane STT and spin-dependent transmission, an observable difference would be found in the angular-dependent in-plane STT at zero temperature and room temperature.

B. Spin dynamics

A macrospin model is used for the spin dynamics in the Ag/Fe(8)/MgO(3)/Fe(8)/MgO(5)/Fe(8)/Ag junction. We assume here the saturation magnetization $M_S = 2.2$ T, corresponding to a magnetic moment of $2.25\mu_B$, uniaxial anisotropy field $\mu_0 H_K = 49.9$ mT, and the intrinsic part of the damping coefficient $\alpha_0 = 0.003$. We also assume that the electrons are fully polarized by the reference magnetization, and the spin current is fully absorbed by the free magnetizations.

TABLE II. In-plane spin transfer torque $\tau^{\parallel}$ in units of $10^{14}\tau_0$ ($\tau_0 \equiv \frac{\hbar}{2e}k\ \Omega^{-1}\,\mathrm{m}^{-2}$) and enhanced magnetic damping $\alpha'_{\theta\theta}$ in the clean Ag/Fe(8)/MgO(3)/Fe(8)/MgO(5)/Fe(8)/Ag DMTJ and Ag/Fe(8)/MgO/Fe(8)/Ag SMTJs with 3 and 5 L MgO barriers with a relative angle of 90° in the absence (presence) of electric bias of 0.1 V at zero and room temperature. For the DMTJ, the effect of interfacial scattering at the Ag/Fe interfaces does not factor in.

Interfaces	0 K					RT			
	$\tau^{\parallel}$	$\Lambda(\uparrow)$	$\Lambda(\downarrow)$	$\alpha'_{\theta\theta}$	Λ	$\tau^{\parallel}$	$\Lambda(\uparrow)$	$\Lambda(\downarrow)$	$\alpha'_{\theta\theta}$
Ag/Fe(8)/MgO(3) in DMTJ	56(63)	2.8(3)	0.8(3)	0.12	3.0	41(60)	2.8(2.6)	0.7(2.6)	4.9×10^{-4}
Ag/Fe(8)/MgO(5) in DMTJ	14(29)	1.25(1)	1.25(1)	2.4×10^{-4}	1.0	12(27)	1.05(1.05)	1.05(1.05)	3.6×10^{-6}
Ag/Fe(8)/MgO(3) in SMTJ	39(129)	0.75(1.2)	25(1.2)	0.046	7.0	−101(−64)	1.5(1.5)	1.5(1.5)	1.1×10^{-4}
Ag/Fe(8)/MgO(5) in SMTJ	0.083(8.3)	0.75(1.1)	5(1.1)	6.9×10^{-4}	4.0	6.0(7.5)	1.0(1.0)	1.0(1.0)	3.5×10^{-6}
Ag/Fe(8)				0.0087					0.0075

Enhanced magnetic damping. The enhanced magnetic damping in the junction with strong interfacial resonant scattering can be sizable [45]. The dynamic exchange coupling, which is well studied and can be parametrized by the enhanced magnetic damping [57–59] in the DMTJs would enrich the spin dynamic behaviors. Table II lists the enhanced magnetic damping α' in the clean Ag/Fe(8)/MgO(3)/Fe(8)/MgO(5)/Fe(8)/Ag junction. When the left-side (right-side) Fe layer is fixed and the other Fe layers are free, we can calculate the α' of the left-side (right-side) Ag/Fe(8)/MgO interface. $\alpha'_{\theta\theta}$ up to 0.12 of the left-side Ag/Fe(8)/MgO(3) interface is found, which is about two orders of magnitude larger than α_0, and about two times larger than that in the clean Ag/Fe(8)/MgO(3)/Fe(8)/Ag junction. The existence of QW resonant scattering should be responsible for the enhancement. The right-side Ag/Fe(8)/MgO(5) interface shows $\alpha'_{\theta\theta} = 2.4\times10^{-4}$, which is the same order as that in the clean Ag/Fe(8)/MgO(5)/Fe(8)/Ag junction, and one order smaller than α_0. Generally, the α' in the MgO-based junction decreases exponentially as the barrier thickness increases. This dependence provides a new parameter to tune the spin dynamics. However, the enhanced magnetic damping along the ϕ direction $\alpha'_{\phi\phi}$ is several orders of magnitude smaller than that along the θ direction. The angular dependence of α' can be fitted by using the asymmetry parameter Λ also. $\Lambda = 3$ and $\Lambda = 1.3$ are found in the left-side Ag/Fe(8)/MgO(3) and right-side Ag/Fe(8)/MgO(5), respectively. Both numbers are considerably smaller than that in the SMTJ with same barrier thickness. The existence of the QW resonant states in the DMTJ should be responsible for the difference.

At higher temperature, the thermal lattice disorder would induce diffusive scattering, which would destroy the specular scattering at the Fe/MgO interfaces and lead to several orders of magnitude reduction in $\alpha'_{\theta\theta}$. At room temperature, $\alpha'_{\theta\theta}$ of the left-side Ag/Fe(8)/MgO(3) interface and right-side Ag/Fe(8)/MgO(5) interface of the DMTJ reduces to 4.9×10^{-4} and 3.6×10^{-6}, respectively. They are the same order as $\alpha'_{\phi\phi}$ and about one order smaller than α_0. The angular dependency of α' at room temperature is completely different from that in zero temperature; $\alpha'_{\phi\phi}$ follows a $\cos^2(\theta/2)$ relation while $\alpha'_{\theta\theta}$ follows a $\sin^2(\theta/2)$ relation. Similar effects are also found in the SMTJ. The magnetic damping would change the switching behavior including the switching time and the critical switching current density and the detail of the spin dynamics structure, which shows more effect on the latter than the former. That is, the spin dynamics structures at room temperature can be noticeably different from that at zero temperature. Here, we pay more attention to on the switching behavior rather than the detail of the spin dynamic structures and we pay more attention to the spin dynamics at zero temperature in the following.

Spin transfer torque. The STT effect in the DMTJ is considerably different from that in the SMTJ [55]. Figure 3 shows the normalized in-plane STT ($h^{\parallel} = \tau^{\parallel}/2KV_F$) in the clean Ag/Fe(8)/MgO(3)/Fe(8)/MgO(5)/Fe(8)/Ag junction under a voltage bias of 0.1 V, where $K = M_sH_k/2$ is the uniaxial anisotropy constant. We observe skewed in-plane STT for both zero and room temperature, and the in-plane STT at zero temperature is larger than that at room temperature. The normalized out-of-plane STT ($h^{\perp} = \tau^{\perp}/2KV_F$) changes the effective field exerted on the magnetization, which is comparably small and shows less effect on the spin dynamic [37,60]. When we pay attention to the switching behavior of the magnetic states rather than the detailed structures of the spin dynamics, we neglect the effect of the out-of-plane STT. The in-plane STT on the left-side Fe $h_L^{\parallel}$ is skewed, and

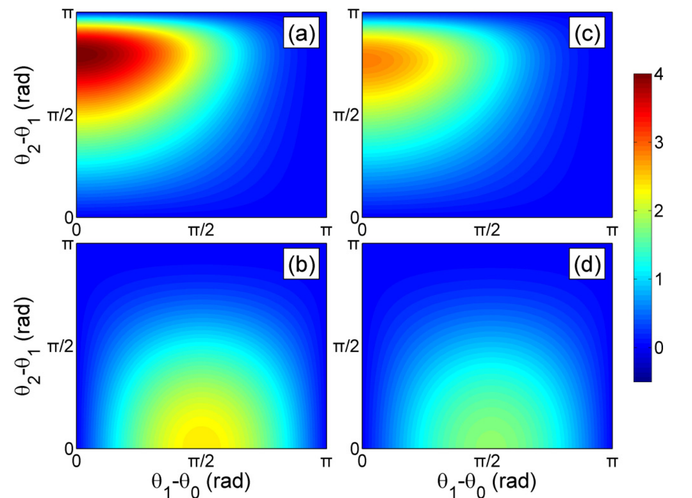

FIG. 3. Normalized in-plane STT $h^{\parallel}$ in the clean Ag/Fe(8)/MgO(3)/Fe(8)/MgO(5)/Fe(8)/Ag DMTJ with bias $V_b = 0.1$ V. Therein, (a)/(c) and (b)/(d) are spin torques on the left- and right-side Fe layers at zero/room temperature.

the functional form can be fitted to an asymmetry parameter [22] with $\Lambda = 3$ (2.6) at zero (room) temperature, as listed in Table II. Comparatively, $\Lambda = 1$ (1.05) is used to fit the in-plane STT on the right-side Fe $h_R^{\parallel}$ at zero (room) temperature. The in-plane STT on the middle-side Fe $h_M^{\parallel}$ is the sum of that on the left-side and right-side Fe layers.

The voltage bias shows a noticeable effect on both the conductance and the STT effect [47,61], as shown in Table II. Our calculations show that a voltage bias of 0.1 V can enhance the conductance in the clean Ag/Fe(8)/MgO(3)/Fe(8)/MgO(5)/Fe(8)/Ag junction from 6.2×10^{11} at equilibrium state to $1.4 \times 10^{12}\ \Omega^{-1}\,\mathrm{m}^{-2}$, and the electrical torquance on the left-side Fe from 56×10^{14} at equilibrium state to $63 \times 10^{14}\tau_0$ ($\tau_0 \equiv \frac{\hbar}{2e}k\ \Omega^{-1}\,\mathrm{m}^{-2}$). For the right-side Fe layer, it is from 14×10^{14} at equilibrium state to $29 \times 10^{14}\tau_0$. Different from finite voltage bias cases, the angular dependency of the zero voltage bias in-plane STT on the left-side Fe at zero (room) temperature can be fitted by two asymmetry parameters with $\Lambda(\uparrow) = 2.8(2.6)$ for the majority spin and $\Lambda(\downarrow) = 0.8(0.7)$ for the minority spin, and one asymmetry parameter $\Lambda = 1.25(1.05)$ for that on the right-side Fe layer.

Compared with the DMTJ, the conductance and STT effect in the SMTJ are more sensitive to the voltage bias. At zero temperature, for the clean Ag/Fe(8)/MgO/Fe(8)/Ag junction with a 3(5) L MgO barrier, the conductance changes from $9.8(0.67) \times 10^{12}$ at the equilibrium state to $8.0(0.40) \times 10^{12}\ \Omega^{-1}\,\mathrm{m}^{-2}$ under voltage bias of 0.1 V, and the electrical torquance from 39(0.083) to $129(8.3) \times 10^{14}\tau_0$, and two asymmetry parameters with $\Lambda(\uparrow) = 0.75(0.75)$ and $\Lambda(\downarrow) = 25(5)$ to one asymmetry parameter $\Lambda = 1.2(1.1)$ for the angular dependency of in-plane STT. At room temperature, the conductance of the clean Ag/Fe(8)/MgO(3)/Fe(8)/Ag is enhanced compared with that at the zero temperature, and a sign reversal of the spin current polarization is found as the temperature changes from zero to room temperature. The sign change would significantly change the spin dynamics in the Ag/Fe(8)/MgO(3)/Fe(8)/MgO(5)/Fe(8)/Ag junction with C3 and C4 structures.

Spin dynamics in the C1 structure. In the C1 structure, the left-side magnetization $\mathbf{M}_0$ is fixed while the middle-side $\mathbf{M}_1$ and right-side $\mathbf{M}_2$ are free. As the conductance of the DMTJ is the function of all the magnetizations, the current-induced spin dynamics in the free magnetizations is dynamically coupled. Figure 4 shows the zero-temperature spin dynamics in the clean Ag/Fe(8)/MgO(3)/Fe(8)/MgO(5)/Fe(8)/Ag junction with C1 structure. For the case with an initial angle θ_2 larger than θ_1 in the presence of a small negative voltage bias, both the $\mathbf{M}_1$ and the $\mathbf{M}_2$ deviate from the north pole and θ_1 increases quicker than θ_2 in the beginning, as shown in the Fig. 3(a), for larger STT on $\mathbf{M}_1$ than on $\mathbf{M}_2$ [55]. As time goes on, $\mathbf{M}_1$ gets close to $\mathbf{M}_2$ and the STT on $\mathbf{M}_2$ begins to decrease. When it is smaller than the damping torque, θ_2 begins to decrease and gets smaller than θ_1. Driven by the damping torque and the increasing negative STT from $\mathbf{M}_2$, θ_1 becomes saturated quickly and then decreases. Finally, both $\mathbf{M}_1$ and $\mathbf{M}_2$ would be stabilized to north pole. As the voltage bias is positive (and the initial angle of θ_2 is larger than θ_1), the STT on both $\mathbf{M}_1$ and $\mathbf{M}_2$ follow the same direction as the

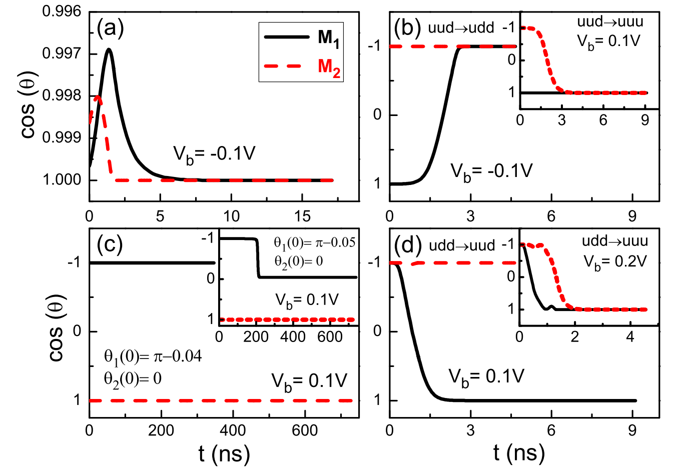

FIG. 4. Zero-temperature spin dynamics in the clean Ag/Fe(8)/MgO(3)/Fe(8)/MgO(5)/Fe(8)/Ag junction with C1 structure.

damping torque, and both $\mathbf{M}_1$ and $\mathbf{M}_2$ would be stabilized to the north pole. For cases with initial angle θ_1 larger than θ_2, we draw the same conclusion. Moreover, the magnitude of the voltage bias shows less effect on the spin dynamics in the C1 structure. That is, the *uuu* structure is dynamically stable.

The dynamically stable *uuu* structure prevents robust manipulation of the magnetic states electronically. However, with the aid of the spin-orbit torque (SOT) effect, four resistance states can be realized in the clean Ag/Fe(8)/MgO(3)/Fe(8)/MgO(5)/Fe(8)/Ag junction with C1 structure via the STT effect. Here the normal metal lead Ag should be replaced by heavy metal Pt, Au, or even layered transition-metal dichalcogenides [62] with large SOC effect. Considering a 3 T structure, a pulse with current density of $2 \times 10^7\ \mathrm{A\,cm^{-2}}$ and duration time 10 ns may be switched from the *uuu* structure to the *uud* structure via the Rashba-Edelstein effect [24,25,62], and vice versa, where a Hall angle of 0.1 and a ratio of 0.1 of out-of-plane spin current to in-plane spin current are used.

The *uud* structure can switch to the *udd* and *uuu* structures via the STT effect induced by a pulse current with voltage bias of 0.1 and 0.2 V, respectively, as shown in Fig. 4(b), corresponding to the current density of $1.2 \times 10^7\ \mathrm{A\,cm^{-2}}$ and $0.6 \times 10^7\ \mathrm{A\,cm^{-2}}$, respectively. Compared with the SOT effect, the switched current density via the STT effect is the same order while the needed switching time is saved. The *udd* structure can switch to *uuu* and *uud* via the STT effect, as shown in Fig. 4(d). It is hard to switch to the the *udu* structure from the *uuu*, *uud*, and *udd* structures via the STT effect. As the deviation of the initial angle θ_1 is larger than 0.05 rad, the *udu* structure can fall into an oscillation state, as shown in Fig. 4(c). So, to switch the *udd* structure to the *udu* structure and vice versa, the SOT effect is needed also.

Figure 5 gives the room-temperature spin dynamics in the clean Ag/Fe(8)/MgO(3)/Fe(8)/MgO(5)/Fe(8)/Ag junction with C1 structure, which is close to the spin dynamics at zero temperature with small difference. Comparing with the spin dynamics at zero temperature, we find that the deterioration of the in-plane STT and magnetic damping by temperature

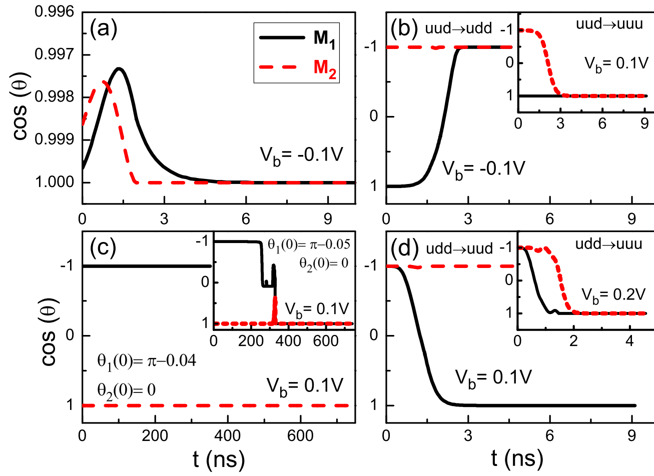

FIG. 5. Room-temperature spin dynamics in the clean Ag/Fe(8)/MgO(3)/Fe(8)/MgO(5)/Fe(8)/Ag junction with C1 structure. Therein, the same initial states as that set in Fig. 4 are taken for comparison.

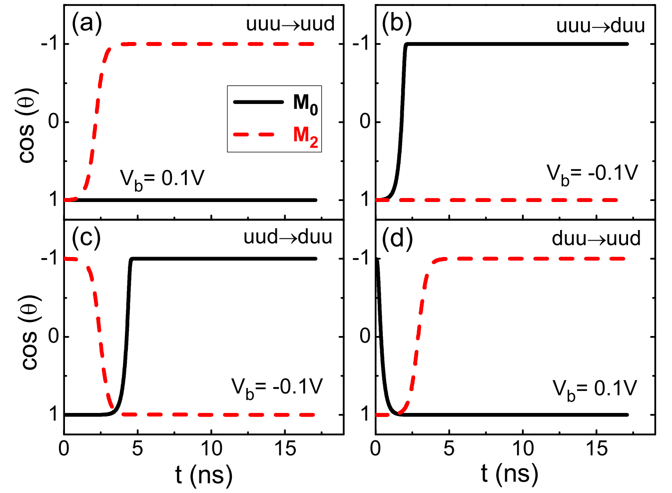

FIG. 6. Zero-temperature spin dynamics in the clean Ag/Fe(8)/MgO(3)/Fe(8)/MgO(5)/Fe(8)/Ag junction with C2 structure.

lengthens the switching time from the *uud*/*udd* state to *udd*/*uud* and *uuu*/*uuu* states as shown in Figs. 5(b) and 5(d). The largest difference lies in the inset of Fig. 5(c), therein a switching from the *udu* state to the *uuu* state is taking place as the initial angle θ_1 is larger than 0.05 rad. The disappearance of the enhanced magnetic damping should be largely responsible for the difference. Generally, the in-plane STT dominates the spin switching behavior in the DMTJ, and the enhanced magnetic damping shows an effect on the detailed structures of spin dynamics.

Spin dynamics in the C2 structure. The difference between the C2 and C1 structures lies in the position of the fixed magnetization. The enhanced magnetic damping affects the spin dynamics in the C2 (and C4) structure with a different manner than that in the C1 (and C3) structure. In the former, the enhanced magnetic damping along the ϕ direction $\alpha'_{\phi\phi}$ affects the spin dynamics along the θ direction while that along the θ direction affects the spin dynamics along the ϕ direction. As $\alpha'_{\phi\phi}$ is orders of magnitude smaller than $\alpha'_{\theta\theta}$, the spin dynamics in the DMTJs with C2 (and C4) structure along the θ direction is dominated by the intrinsic magnetic damping constant rather than $\alpha'_{\phi\phi}$. That is, the enhanced magnetic damping shows less effect on the spin dynamics in the C2 (and C4) structure compared with the C1 (and C3) structure. So, we observe that the zero-temperature spin dynamics in the DMTJs with C2 (and C4) structure are almost same as that at room temperature.

The spin dynamics of the free magnetizations in the C2 structure are dynamically coupled also. Figure 6 gives the zero-temperature spin dynamics in the clean Ag/Fe(8)/MgO(3)/Fe(8)/MgO(5)/Fe(8)/Ag junction with C2 structure driven via the STT effect. A pulse with voltage bias of 0.1 V and −0.1 V would be sufficient to switch the *uuu* structure to the *uud* and *duu* structures, respectively, as shown in Figs. 6(a) and 6(b), and switch the *uud* and *duu* structures to the *duu* and *uud* structures, respectively, as shown in Figs. 6(c) and 6(d). By carefully controlling the duration time, both the *uud* and the *duu* structures can switch to the *uuu* structure. However, it is impossible to switch the *uuu*, *duu*, and *uud* structures to the *dud* structure via the STT effect. That is, three resistance states can be achieved in the Ag/Fe(8)/MgO(3)/Fe(8)/MgO(5)/Fe(8)/Ag junction with C2 structure only via the STT effect.

Spin dynamics in the C3 and C4 structures. Both the C3 and the C4 structures can be considered as two SMTJs in series. The joining of independent voltage biases on the free magnetizations expands the parameter space of the spin dynamics, leading to rich spin dynamics behaviors in the C3 structure compared with the C1 structure. The spin dynamics in the C4 structure can be considered as a simple superposition of two independent spin dynamics in the SMTJs.

Table III summarizes the switching behaviors in the clean Ag/Fe(8)/MgO(3)/Fe(8)/MgO(5)/Fe(8)/Ag junction with C3 and C4 structures. For the junction with C3 structure, as

TABLE III. Magnetic switch in the clean Ag/Fe(8)/MgO(3)/Fe(8)/MgO(5)/Fe(8)/Ag junction with C3 and C4 structures at zero (room) temperature. Therein, V_{b1} and V_{b2} are two independent voltage biases exerted on the left side and right side, respectively, and t_p is the switching time. The upper (lower) sign corresponds to the switch from the left (right) structure to the right (left) structure.

Behavior	V_{b1} (V)	V_{b2} (V)	t_p (ns)
	C3 structure		
uuu ⇌ *uud*	0.02(−0.02)	∓0.1(∓0.1)	18(24)
uuu ⇌ *udd*	∓0.02(±0.02)	0.1(0.1)	16(22)
uud ⇌ *udd*	∓0.02(±0.02)	0(0)	17(24)
udu ⇌ *udd*	−0.02(0.02)	∓0.1(±0.1)	18(19)
	C4 structure		
uuu ⇌ *uud*	<0.0011(>−0.0023)	±0.1(±0.1)	18(19)
uuu ⇌ *duu*	±0.01(∓0.01)	<0.014(<0.015)	18(24)
uuu ⇌ *dud*	±0.01(∓0.01)	±0.1(±0.1)	18(24)
uud ⇌ *duu*	±0.01(∓0.01)	∓0.1(∓0.1)	18(24)
uud ⇌ *dud*	±0.01(∓0.01)	>−0.014(>−0.015)	18(24)
duu ⇌ *dud*	>−0.0011(<−0.0023)	±0.1(±0.1)	18(19)

the right-side voltage bias V_{b2} is set at 0.1 V and the ratio V_{b1}/V_{b2} is set at 0.2, four reversible switching processes are found with the switching time around 18 ns at zero temperature and 24 ns at room temperature. They are switching from the *uuu* state to the *uud* and *udd* states and vice versa, and from the *udd* state to the *uud* and *udu* states and vice versa. Four resistance states can be fully realized by the combination of these four reversible switching processes. The increase of V_{b1} and V_{b2} would shorten the needed duration time. The decrease of V_{b1} and V_{b2}, especially when V_{b2} is within range from 0.018 to 0.05 V, would induce an oscillation state at zero temperature. Reversible switching from the *uud* state to the *udu* state directly is hard to realize at both zero and room temperatures, and the switching from the *uuu* state to the *udu* state can be realized at room temperature only.

For the C4 structure, four resistance states can directly switch to each other reversibly, and no oscillation states are found at both zero temperature and room temperature. At zero temperature, for Ag/Fe(8)/MgO/Fe(8)/Ag junctions with three and five L MgO barriers, the critical switching bias is around 0.0011 V and 0.014 V s, respectively. At room temperature, it is around 0.0023 and 0.015 V, respectively. Taking $V_{b1} = 0.01$ V and $V_{b2} = 0.1$ V, the switching time is around 18 ns at zero temperature and 24 ns at room temperature.

IV. SUMMARY

We calculate the resistance states and spin dynamics in the asymmetric Ag/Fe(8)/MgO(3)/Fe(8)/MgO(5)/Fe(8)/Ag DMTJ from first principles. Four resistance states with noticeable difference are found therein. Rich spin dynamics behaviors originated from the larger parameter space compared with SMTJ are found, and three and four resistance states can be realized via modulating the voltage bias scheme and the position of the reference magnetization. Based on our results, we show that asymmetric MgO-based DMTJs could serve as a basic circuit element for the implementation of base-3 and base-4 algorithms.

ACKNOWLEDGMENTS

We gratefully acknowledge financial support from the National Natural Science Foundation of China (Grants No. 11274094, No. 11804062, No. 51772076, No. U1804165, and No. 11805052) and Henan Polytechnic University (Grant No. B2012-021). H.T. acknowledges financial support from the Natural Science Foundation of Guangxi under Grant No. 2017JJA110297y, and Guangxi Normal University under Grant No. 20172D010.

[1] P. Krzysteczko, G. Reiss, and A. Thomas, Appl. Phys. Lett. **95**, 1450 (2009).
[2] J. P. Velev, C.-G. Duan, J. D. Burton, A. Smogunov, M. K. Niranjan, E. Tosatti, S. S. Jaswal, and E. Y. Tsymbal, Nano Lett. **9**, 427 (2009).
[3] M. Gajek, M. Bibes, S. Fusil, K. Bouzehouane, J. Fontcuberta, A. Barthélémy, and A. Fert, Nat. Mater. **6**, 296 (2007).
[4] A. Thomas, P. Krzysteczko, J. Münchenberger, G. Reiss, and M. Schäfers, Adv. Mater. **24**, 762 (2012).
[5] G. Indiveri, B. Linares-Barranco, R. Legenstein, G. Deligeorgis, and T. Prodromakis, Nanotechnology **24**, 384010 (2013).
[6] N. Locatelli, V. Cros, and J. Grollier, Nat. Mater. **13**, 11 (2014).
[7] X. Zhang, W. Cai, X. Zhang, Z. Wang, Z. Li, Y. Zhang, K. Cao, N. Lei, W. Kang, Y. Zhang *et al.*, ACS Appl. Mater. Interfaces **10**, 16887 (2018).
[8] Y. Zhang, L. Zhang, W. Wen, G. Sun, and Y. Chen, in *2012 IEEE/ACM International Conference on Computer-Aided Design (ICCAD)* (IEEE, 2012), pp. 526–532.
[9] Y. Luo and G. F. Ernult, Magnetoresistive device and a writing method for a magnetoresistive device, U.S. Patent No. 9058885, June 16, 2015.
[10] A. Chanthbouala, R. Matsumoto, J. Grollier, V. Cros, A. Anane, A. Fert, A. V. Khvalkovskiy, K. A. Zvezdin, K. Nishimura, and Y. Nagamine, Nat. Phys. **7**, 626 (2011).
[11] T. Yoo, S. Khym, H. Lee, S. Lee, S. Kim, J. Shin, S. Lee, X. Liu, and J. Furdyna, J. Nanosci. Nanotechnol. **11**, 5990 (2011).
[12] S. H. Jo, T. Chang, I. Ebong, B. B. Bhadviya, P. Mazumder, and W. Lu, Nano Lett. **10**, 1297 (2010).
[13] C. M. Liyanagedera, A. Sengupta, A. Jaiswal, and K. Roy, Phys. Rev. Appl. **8**, 064017 (2017).
[14] A. Sengupta and K. Roy, Phys. Rev. Appl. **5**, 024012 (2016).
[15] J. Grollier, D. Querlioz, and M. D. Stiles, Proc. IEEE **104**, 2024 (2016).
[16] J. Torrejon, M. Riou, F. A. Araujo, S. Tsunegi, G. Khalsa, D. Querlioz, P. Bortolotti, V. Cros, K. Yakushiji, A. Fukushima *et al.*, Nature (London) **547**, 428 (2017).
[17] S. Hurst, IEEE Trans. Comput. **33**, 1160 (1984).
[18] E. Dubrova, in *Proceedings of NORCHIP* (IEEE, 1999), Vol. 99, pp. 340–350.
[19] J. Shim, S. Oh, D.-H. Kang, S.-H. Jo, M. H. Ali, W.-Y. Choi, K. Heo, J. Jeon, S. Lee, M. Kim *et al.*, Nat. Commun. **7**, 13413 (2016).
[20] A. Konar, *Artificial Intelligence and Soft Computing: Behavioral and Cognitive Modeling of the Human Brain* (CRC Press, Boca Raton, FL, 1999).
[21] L. Britnell, R. Gorbachev, A. Geim, L. Ponomarenko, A. Mishchenko, M. Greenaway, T. Fromhold, K. Novoselov, and L. Eaves, Nat. Commun. **4**, 1794 (2013).
[22] J. C. Slonczewski, J. Magn. Magn. Mater. **159**, L1 (1996).
[23] L. Berger, Phys. Rev. B **54**, 9353 (1996).
[24] I. M. Miron, K. Garello, G. Gaudin, P.-J. Zermatten, M. V. Costache, S. Auffret, S. Bandiera, B. Rodmacq, A. Schuhl, and P. Gambardella, Nature (London) **476**, 189 (2011).
[25] L. Liu, C.-F. Pai, Y. Li, H. W. Tseng, D. C. Ralph, and R. A. Buhrman, Science **336**, 555 (2012).
[26] L. Liu, O. J. Lee, T. J. Gudmundsen, D. C. Ralph, and R. A. Buhrman, Phys. Rev. Lett. **109**, 096602 (2012).
[27] S. Fukami, C. Zhang, S. DuttaGupta, A. Kurenkov, and H. Ohno, Nat. Mater. **15**, 535 (2016).
[28] M. Cubukcu, O. Boulle, M. Drouard, K. Garello, C. O. Avci, I. M. Miron, J. Langer, B. Ocker, P. Gambardella, and G. Gaudin, Appl. Phys. Lett. **104**, 042406 (2014).

[29] X. Zhang, C. H. Wan, Z. H. Yuan, Q. T. Zhang, H. Wu, L. Huang, W. J. Kong, C. Fang, U. Khan, and X. F. Han, Phys. Rev. B **94**, 174434 (2016).
[30] L. You, O. Lee, D. Bhowmik, D. Labanowski, J. Hong, J. Bokor, and S. Salahuddin, Proc. Natl. Acad. Sci. USA **112**, 10310 (2015).
[31] Y.-C. Lau, D. Betto, K. Rode, J. Coey, and P. Stamenov, Nat. Nanotechnol. **11**, 758 (2016).
[32] A. van den Brink, G. Vermijs, A. Solignac, J. Koo, J. T. Kohlhepp, H. J. Swagten, and B. Koopmans, Nat. Commun. **7**, 10854 (2016).
[33] K. Cai, M. Yang, H. Ju, S. Wang, Y. Ji, B. Li, K. W. Edmonds, Y. Sheng, B. Zhang, N. Zhang *et al.*, Nat. Mater. **16**, 712 (2017).
[34] M. DC, R. Grassi, J.-Y. Chen, M. Jamali, D. Reifsnyder Hickey, D. Zhang, Z. Zhao, H. Li, P. Quarterman, Y. Lv *et al.*, Nat. Mater. **17**, 800 (2018).
[35] M. Wang, W. Cai, D. Zhu, Z. Wang, J. Kan, Z. Zhao, K. Cao, Z. Wang, Y. Zhang, T. Zhang *et al.*, Nat. Electron. **1**, 582 (2018).
[36] S. Shi, Y. Ou, S. V. Aradhya, D. C. Ralph, and R. A. Buhrman, Phys. Rev. Appl. **9**, 011002 (2018).
[37] J. Z. Sun, Phys. Rev. B **62**, 570 (2000).
[38] A. Brataas, G. E. Bauer, and P. J. Kelly, Phys. Rep. **427**, 157 (2006).
[39] K. M. D. Hals, A. Brataas, and Y. Tserkovnyak, Europhys. Lett. **90**, 47002 (2010).
[40] A. Brataas, Y. Tserkovnyak, and G. E. W. Bauer, Phys. Rev. Lett. **101**, 037207 (2008).
[41] Y. Tserkovnyak, A. Brataas, and G. E. W. Bauer, Phys. Rev. B **66**, 224403 (2002).
[42] A. Brataas, Y. Tserkovnyak, and G. E. W. Bauer, Phys. Rev. B **84**, 054416 (2011).
[43] H. Ebert, S. Mankovsky, D. Ködderitzsch, and P. J. Kelly, Phys. Rev. Lett. **107**, 066603 (2011).
[44] Q. Liu, H. Yuan, K. Xia, and Z. Yuan, Phys. Rev. Mater. **1**, 061401 (2017).
[45] H.-M. Tang and X.-T. Jia, Phys. Rev. Appl. **10**, 024042 (2018).
[46] I. Turek, V. Drchal, J. Kudrnovskỳ, M. Sob, and P. Weinberger, *Electronic Structure of Disordered Alloys, Surfaces and Interfaces* (Kluwer, Boston, 1997).
[47] Y. Ke, K. Xia, and H. Guo, Phys. Rev. Lett. **105**, 236801 (2010).
[48] X. Jia, K. Xia, and G. E. W. Bauer, Phys. Rev. Lett. **107**, 176603 (2011).
[49] B. Ricco and M. Y. Azbel, Phys. Rev. B **29**, 1970 (1984).
[50] Y. Wang, Z.-Y. Lu, X.-G. Zhang, and X. F. Han, Phys. Rev. Lett. **97**, 087210 (2006).
[51] D. Herranz, F. G. Aliev, C. Tiusan, M. Hehn, V. K. Dugaev, and J. Barnaś, Phys. Rev. Lett. **105**, 047207 (2010).
[52] R. S. Liu, S.-H. Yang, X. Jiang, X.-G. Zhang, C. Rettner, L. Gao, T. Topuria, P. M. Rice, W. Zhang, C. M. Canali *et al.*, Phys. Rev. B **87**, 024411 (2013).
[53] S. Ikeda, K. Miura, H. Yamamoto, K. Mizunuma, H. Gan, M. Endo, S. Kanai, J. Hayakawa, F. Matsukura, and H. Ohno, Nat. Mater. **9**, 721 (2010).
[54] H. X. Yang, M. Chshiev, B. Dieny, J. H. Lee, A. Manchon, and K. H. Shin, Phys. Rev. B **84**, 054401 (2011).
[55] X. Jia, S. Wang, and M. Qin, New J. Phys. **18**, 063012 (2016).
[56] S. Yuasa, T. Nagahama, A. Fukushima, Y. Suzuki, and K. Ando, Nat. Mater. **3**, 868 (2004).
[57] B. Heinrich, Y. Tserkovnyak, G. Woltersdorf, A. Brataas, R. Urban, and G. E. W. Bauer, Phys. Rev. Lett. **90**, 187601 (2003).
[58] J. Li, L. R. Shelford, P. Shafer, A. Tan, J. X. Deng, P. S. Keatley, C. Hwang, E. Arenholz, G. van der Laan, R. J. Hicken *et al.*, Phys. Rev. Lett. **117**, 076602 (2016).
[59] H. J. Jiao and G. E. W. Bauer, Phys. Rev. Lett. **110**, 217602 (2013).
[60] P. Ogrodnik, G. E. W. Bauer, and K. Xia, Phys. Rev. B **88**, 024406 (2013).
[61] X. Jia, K. Xia, Y. Ke, and H. Guo, Phys. Rev. B **84**, 014401 (2011).
[62] Q. Shao, G. Yu, Y.-W. Lan, Y. Shi, M.-Y. Li, C. Zheng, X. Zhu, L.-J. Li, P. K. Amiri, and K. L. Wang, Nano Lett. **16**, 7514 (2016).